Correspondence to:

A. Supply,
alexandre.supply@univ-brest.fr

Meltwater Lenses Over the Chukchi and the Beaufort Seas During Summer 2019: From In Situ to Synoptic View

Alexandre Supply[1,2] , **Jacqueline Boutin[3]** , **Nicolas Kolodziejczyk[1]** , **Gilles Reverdin[3]** , **Camille Lique[1]** , **Jean-Luc Vergely[4], and Xavier Perrot[5]**

[1]University Brest, CNRS, IRD, Ifremer, Laboratoire d'Océanographie Physique et Spatiale (LOPS), IUEM, Brest, France, [2]CNES, Paris, France, [3]Sorbonne University, LOCEAN Laboratory—IPSL, CNRS–IRD–MNHM, Paris, France, [4]ACRI-ST, Guyancourt, France, [5]LMD/IPSL, CNRS, ENS, PSL, Paris, France

Abstract We investigate the Chukchi and the Beaufort seas in the Arctic Ocean, where salty and warm Pacific Water flows in through the Bering Strait and interacts with the sea ice, contributing to its summer melt. Thanks to in situ measurements recorded by two saildrones deployed during summer 2019 and to refined sea ice filtering in satellite L-band radiometric data, we demonstrate the ability of satellite sea surface salinity (SSS) observed by Soil Moisture and Ocean Salinity and Soil Moisture Active and Passive to capture SSS freshening induced by sea ice melt. We refer to these freshening events as meltwater lenses (MWL). The largest MWL observed by the saildrones during this period occupied a large part of the Chukchi shelf, with a SSS freshening reaching −5 practical salinity scale, persisting for up to 1 month. This MWL restricted the transfer of air-sea momentum to the upper ocean, as illustrated by measured wind speed and vertical profiles of currents. With satellite-based sea surface temperature, satellite SSS provides a monitoring of the different water masses encountered in the region during summer 2019. Using sea ice concentration and estimated Ekman transport, we analyze the spatial variability of sea surface properties after the sea ice edge retreat over the Chukchi and the Beaufort seas. The two MWL captured by the saildrones and the satellite measurements resulted from different dynamics. Over the Beaufort Sea, the MWL evolution followed the meridional sea ice retreat whereas, in the Chukchi Sea, a large persisting MWL was generated by advection and subsequent melting of a sea ice filament.

Plain Language Summary The Arctic Ocean is an area of large variations in salinity. Salinity is a main driver of ocean circulation as it determines (with seawater temperature) the seawater density. However, very little is known about salinity variations there, due to the paucity of measurements near ice and in river plumes where surface water is freshest. Here, we use surface salinity measurements from two autonomous vehicles, named saildrones, to show that satellite measurements can identify the evolution of freshwater lenses that result from sea ice melt. Over the Chukchi and the Beaufort seas, sea surface salinity exhibits large seasonal changes, partly because of the sea ice melting. In this region, water from the North Pacific Ocean enters the Arctic Ocean, resulting in large gradients of salinity and temperature. During summer 2019, the saildrones measured the surface salinity and temperature variability as the sea ice retreated northwards. By comparing these data with the measurements from satellites, we showed that satellites can detect these pools of fresh surface water in the Arctic Ocean, increasing the field of application of satellites to understand changes in conditions that determine the Arctic's role in climate change.

1. Introduction

The Arctic Ocean surface salinity is largely influenced by river discharges and sea ice melting. As in any cold environment, salinity largely determines the seawater density structure which, in turn, controls the ocean dynamics and vertical mixing. In the Arctic Ocean, Pacific Water (PW), which enters through the Bering Strait to the Chukchi Sea, is one of the primary low salinity sources. Over the Chukchi Shelf, two distinct Pacific-originated water masses are commonly observed: the relatively salty Bering Sea Water (BSW; between 32 and 33 practical scale salinity (pss)) and the relatively fresh Alaskan Coastal Water (ACW; between 31 and 32 pss; Coachman et al., 1975; Steele et al., 2004). ACW is mainly composed of Riverine Water (RW), with a strong contribution from the Yukon River. ACW and the easternmost branch of BSW are injected into the Beaufort Gyre trough Barrow Canyon, while the westernmost branch is advected northward and carries PW toward the Transpolar Drift (Timmermans et al., 2014).

Woodgate and Peralta-Ferriz (2021) reported on an increase of the PW transport into the Chukchi Sea since 1990, associated with an increase of the heat inflow. This trend is a part of the "borealization" affecting the Arctic Ocean (Polyakov et al., 2020). These changes have significant consequences on sea ice spatial and temporal variability (Danielson et al., 2020).

As PW brings heat to the Arctic during spring and summer, it contributes to the seasonal sea ice melt. This source of warm water may take the form of a jet penetrating into the Arctic Ocean up to the Beaufort Sea, passing by the Barrow Canyon (MacKinnon et al., 2021). As sea ice melts and retreats, the large amount of freshwater added to the sea surface may induce a strong decrease in sea surface salinity (SSS) following the sea ice edge retreat during summer. This freshening could be correlated with the distance from the sea ice edge, as described by Dewey et al. (2017) for the Beaufort Sea. These lenses strongly modify the surface density and thus influence ocean dynamics. Induced strong stratification also influences ocean-sea-ice-atmosphere exchanges. The stratification further impacts the near surface temperature maximum ability to store summer heat during winter and then to influence sea ice melting the following summer (Steele et al., 2011).

Nevertheless, due to their sporadic nature and the difficulty of sea surface monitoring over the Arctic Ocean, these freshening events remain poorly documented. In this context, autonomous vehicles provide valuable information. In summer 2019, saildrones were deployed for the first time in the vicinity of sea ice in the Chukchi and Beaufort seas (Vazquez-Cuervo et al., 2021). Saildrones provide key measurements of salinity and temperature close to the ocean surface (at about 0.5 m depth). The ability of saildrones to measure wind speed (WS) and ocean currents is key to studying how the surface freshening induced by sea ice melt evolves and can influence air-sea exchanges. In addition, satellite estimates, while less accurate than in situ measurements provided by saildrones, offer a unique synoptic view.

The Soil Moisture and Ocean Salinity (SMOS; 2010-present, Font et al., 2010; Kerr et al., 2010) and the Soil Moisture Active and Passive (SMAP; 2015-present, Piepmeier et al., 2017) satellites both monitor SSS at a resolution close to 43 km with a temporal sampling close to 1 day at very high latitudes (Reul et al., 2020; Vinogradova et al., 2019). The low sea surface temperature (SST) values characteristic of the Arctic Ocean results in a poor sensitivity of L-band radiometric measurements to SSS (Meissner et al., 2016). Despite this poor sensitivity, which is somewhat compensated by very large SSS contrasts in the Arctic that range from 35 pss for the Atlantic water to 0 pss for river plumes (Carmack et al., 2016), satellite SSS data have been used to characterize surface water masses in the Arctic Ocean (Olmedo et al., 2018; Tang et al., 2018). With the use of complementary variables, such as SST and Colored Dissolved Organic Matter, provided by satellites such as the Advanced Microwave Scanning Radiometer (AMSR)-2, SSS may also allow for the monitoring of sea surface variability in Arctic river plumes at intra-seasonal scales (Matsuoka et al., 2016; Tarasenko et al., 2021). The long SMOS time series enables investigating inter-annual variability (Supply et al., 2020a). Nevertheless, numerous challenges remain regarding satellite-derived SSS estimates in the Arctic Ocean. Due to sparse in situ measurements, correcting satellites values using in situ derived SSS and an optimal interpolation method remains difficult (Kolodziejczyk et al., 2021). An additional limitation comes from the sea ice heterogeneity and instrument resolution, limiting the measurements closer than ~43 km from the ice edge, with difficulties in detecting and filtering small ice-covered regions. Furthermore, sea ice presence in a satellite pixel has the potential to significantly contaminate the retrieved satellite SSS. As an example, considering a brightness temperature of sea ice twice the one of sea water, a coverage of 0.2% of the surface of the considered pixel by sea ice would lead to a SSS underestimate of ~1 pss. Hence, a first important step in our paper is to assess the ability of L-band radiometers on satellites to monitor from space freshening induced by sea ice melt forming meltwater lenses (MWL). This is performed by comparing SMOS and SMAP SSS with the measurements from two saildrones in the vicinity of sea ice.

We describe data and methods we followed in Section 2. Vazquez-Cuervo et al. (2021) demonstrated the good agreement between SMAP SSS and saildrones SSS, with a particularly good monitoring of the Yukon River plume during summer 2019. Here, measurements carried out from the same saildrone campaign close to the sea ice are used to assess the ability of both SMOS and SMAP satellite data to monitor the SSS decrease induced by sea ice melt over the Chukchi and the Beaufort Sea (Section 3). We then discuss saildrone measurements of SSS and SST for the largest MWL crossed by the saildrones, as well as WS and current measurements (Section 4). Finally, we present the evolution of sea surface properties in the Chukchi and the Beaufort seas using satellite measurements in Section 5. We discuss the results and conclude in Section 6.
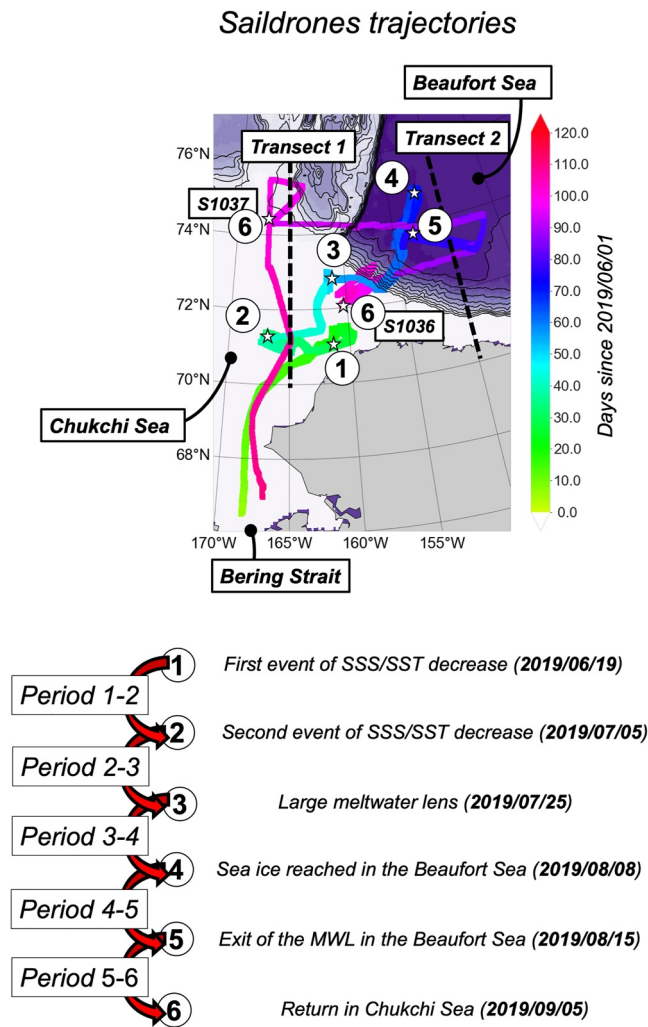
Saildrones trajectories

Figure 1. Saildrones trajectory (colors corresponding to the day number) overlayed on bathymetry. The numbers indicate the various stages described in the text. The positions of the transects shown on Figures 7 and 8 are indicated with dashed lines—background colors indicate the bathymetry.

2. Data and Methods

The present study is limited to a period from June to September 2019. Thus, in the following, day number corresponds to the number of days since 1 June 2019.

2.1. In Situ Measurements From Saildrones

2.1.1. Sea Surface Salinity (SSS) and Sea Surface Temperature (SST)

Saildrones are wind-powered oceanographic autonomous devices that can travel over long distances (Mordy et al., 2017). During summer 2019, two saildrones (saildrones 1036 and 1037, hereafter S1036 and S1037) were deployed in the Arctic Ocean as part of the National Oceanographic Partnership Program (NOPP)—Multi Sensor Improved SST (MISST) project. Figure 1 illustrates their trajectory from June to September. Saildrones are equipped with two Conductivity-Temperature-Depth sensors: aE SBE37 sensor at 60-cm depth and an RBR sensor at 53-cm depth. Each sensor provides a salinity value each minute (with each minute 12-s average of at 1 Hz-sampled measurements). A systematic bias of 0.17 pss was recorded between the salinities measured by the SBE37 and the RBR. Due to an unexplained large decrease in salinity on the SBE37 sensor, we choose to use the RBR salinity for comparisons with satellite SSS estimates, similar to Vazquez-Cuervo et al. (2021).

2.1.2. Currents

In addition to salinity and temperature measurements, we also use current estimates from 300 kHz Teledyne Workhorse Monitor WHM300 Acoustic Doppler Current Profiler (ADCP) systems on both saildrones.

The temporal resolution of the current estimates is 5 min with the shallowest level at 4.2 m and the deepest at 102.2 m, and with a 2-m vertical resolution. From the currents measured at different depths, we derive the vertical shear between surface and deeper currents as:

$$\text{Shear} = \sqrt{\left(\frac{\partial u(z)}{\partial z}\right)^2 + \left(\frac{\partial v(z)}{\partial z}\right)^2} \tag{1}$$

With $u(z)$ and $v(z)$ being the zonal and meridional components of ocean velocity.

2.1.3. Wind Speed and Direction

To study the effect of the wind on the ocean surface and to derive estimates of Ekman transport, we use wind measurements derived from a Gill Anemometer mounted at the top of the saildrone mast at 5 m height, and averaged over a minute. In previous studies, saildrone WS measurements demonstrate a root mean square difference with other in situ measurements of close to 0.6 m s^{-1} (Gentemann et al., 2020).

2.2. Satellite Measurements

2.2.1. Sea Surface Salinity (SSS)

We use SSS weekly fields derived from SMOS and SMAP measurements. We build weekly SMOS SSS fields from level 2 data as described below, and use weekly SMAP SSS fields provided by Jet Propulsion Laboratory (JPL). Both products are daily oversampled. SMOS weekly SSS are derived following a methodology following Supply et al. (2020a) to minimize the error associated with the sea ice presence and to affect, as little as possible, the SSS variability derived from the satellite measurements.

SMOS SSS comes from a modified version of the CEC-LOCEAN L3 Arctic, distributed by the Center Aval de Traitement des Données SMOS (CATDS; Supply et al., 2020b). In this new version, the SMOS level 2 SSS are from the European Space Agency Climate Change Initiative v3.2 reprocessing described by Perrot et al. (2021). In comparison with level 2 SSS used in Supply et al. (2020a), level 2 SSS used here differs in the following ways: (a) it is computed with an updated dielectric constant parametrization (Boutin et al., 2020); (b) the SMOS vicarious calibration, the so-called Ocean Target Transformation, is derived using Argo optimal interpolated SSS (Gaillard et al., 2016) instead of a climatology; and (c) SST and WS used as priors in the SSS retrieval are taken from European Center for Medium-Range Weather Forecasts (ECMWF) ERA5 instead of ECMWF forecasted fields. With respect to the methodology described in Supply et al. (2020a), we update the sea ice filtering derived from the difference between the SMOS-retrieved pseudo dielectric constant (Acard parameter) and the one expected from retrieved SSS and SST: instead of being applied only at level 3, sea ice filtering is applied both at level 2 (swath product) and at level 3 (weekly averaged product), which provides more consistent results when compared with the saildrone data.

SMOS SSS values are averaged over 9 days on a 25 km Equal-Area Scalable Earth (EASE) 2.0 grid adapted to polar areas. These fields have an effective spatial resolution close to 50 km, corresponding to the original resolution of SMOS SSS (no spatial interpolation is applied from level 2 to level 3). SSS is derived with a correction of SST-induced bias using remote sensing systems (RSS) SST. Given the difficulty of finding a reference to adjust absolute SSS values in the Arctic Ocean, this product does not contain any Land Sea Contamination (LSC) correction; nevertheless, in the averaging process, SMOS SSS is weighted by the cost function of the retrieval (Chi2), and we expect it to be degraded on the satellite swath parallel subdivisions (dwell lines) largely contaminated by LSC.

When compared with saildrone measurements, this SMOS SSS product performs better than the BEC Arctic product v3.1 (Martinez et al., 2022): the standard deviation of the difference (STDD) is increased up to 8% with the BEC product (comparisons are shown in Figure S1 in Supporting Information S1).

For SMAP, we use the (JPL; Fore et al., 2019) version 4.3 8-day averaged SSS provided on a 0.25° regular grid, with a spatial interpolation from level 2 to level 3. In this product that uses a LSC correction, the effective spatial resolution of SSS is close to 60 km. The use of JPL SMAP SSS instead of SMAP SSS v4 distributed by RSS is motivated by a less restrictive ice mask in the polar regions. Between 19th June and 23 July 2019, SMAP was in safe mode and did not provide SSS estimates.

SMOS and SMAP SSS are provided with uncertainties estimated by the SSS retrieval algorithm.

An additional filtering (mainly removing pixels contaminated by sea ice) is applied considering SMOS and SMAP SSS retrieval uncertainties (see Figure S2 in Supporting Information S1—only SSS estimates with an uncertainty lower than 0.6 pss are considered in the following). SSS estimates from both satellites are intercalibrated using saildrone measurements: the mode of the distribution between each satellite SSS and saildrone SSS allows us to define a constant correction applied to SMOS and SMAP. Four our data, 0.5 pss are added to SMOS SSS and 0.5 pss are subtracted from SMAP SSS. After the filtering, SMOS and SMAP SSS are finally combined in one product: SMOS + SMAP SSS, by averaging the values of the two satellites, without any weighting by the uncertainty. Prior to this operation, SMAP is interpolated to the same 25 km EASE 2.0 grid as SMOS. These two latter steps ensure an equivalent weight of the two satellite data sets in the average. Nevertheless, there is an exception: when a pixel is not covered by a measurement from one satellite (due, e.g., to different behaviors of the sea ice filtering), only the measurement from the other satellite is used. Thus, between 19th June and July 23rd, SMOS + SMAP SSS corresponds to SMOS SSS. We also derive an error estimate for this combined SSS product based on the uncertainties from SMOS and SMAP. This product is available on the SEANOE website (Supply et al., 2022).

Figure S3 in Supporting Information S1 illustrates comparisons between saildrone salinity and SSS retrieved with SMOS, SMAP or SMOS + SMAP combined products. SMOS SSS estimates are noisier than SMAP SSS estimates (Figure S3 in Supporting Information S1; see also satellite-saildrone differences in Figure S2 in Supporting Information S1). Nevertheless, SMOS provides a better consistency than SMAP between satellite estimates and in situ measurements considering salinities lower than 28 pss on one side and higher than 28 pss one the other side. The mean of the difference (MoD) recorded between SMAP and saildrone is 0.32 pss above 28 and 0.00 pss below. The Difference of MoD is lower between SMOS and saildrones: −0.15 above 28 pss and −0.10 below

28 pss. SMOS and SMAP instruments and retrieval methodologies present differences (including different geometry of acquisition and prior information) that induce a different filtering of sea ice (some pixels are filtered with SMOS and not with SMAP, and inversely). Combining both products allows us to reduce the noise, increase the spatio-temporal coverage and retain the higher consistency of SMOS SSS.

2.2.2. Sea Surface Temperature (SST)

We use the SST product provided by RSS (http://www.remss.com/measurements/sea-surface-temperature/oisst-description/), which combines infrared and microwave data with an optimal interpolation. SST is provided at 9 km resolution, and then linearly interpolated on the EASE grid with a 25 km resolution.

2.2.3. Sea Ice Concentration (SIC)

We use the Ocean and Sea Ice Satellite Application Facility Sea Ice Concentration (SIC) derived from AMSR-2 measurements, provided by the Danish and the Norwegian Meteorological Institutes. The AMSR-2 instrument is a dual-polarized and conically scanning microwave radiometer with eight channels from 6.93 to 89.00 GHz which can be used to retrieve various geophysical parameters, such as rain rate, WS and SST. The Hybrid Dynamic (OSHD) algorithm operated for OSI SAF SIC retrieval uses 18.70, 36.50, and 89.00 GHz bands with spatial resolution 22×14, 12×7, and 5×3 km respectively. Close to the sea ice edge, SIC estimates tend to be more uncertain in thin ice conditions or when floe sizes are not resolved by microwave radiometers (Liu et al., 2016). This limits the use of microwave radiometers to estimate SIC for filtering sea ice in L-band SSS retrieval, as L-band measurements are more sensitive to thin ice than measurements at higher frequencies.

2.3. Atmospheric Reanalysis

To derive Ekman transport, we use ECMWF ERA5 winds (zonal and meridional components, U_{ERA5} and V_{ERA5}) and ERA5 air density (ρ_{ERA5}) provided by Copernicus Climate Change Service (C3S, Hersbach et al., 2020).

2.4. Methodology

2.4.1. Collocations

Satellite, reanalysis estimates and in situ measurements are collocated within a 1-day temporal radius (considering the central day for the satellite weekly products). All in situ measurements present in a satellite/reanalysis pixel are averaged to correspond to one satellite (or reanalysis) estimate, which results in a non-regular temporal time step for time series, depending on the saildrone trajectory and product grid. After collocation, in situ, reanalysis and satellite time series are linearly interpolated onto a regular temporal grid with a one-hour time step to investigate the consistency between the different sources of observations.

2.4.2. Ekman Transport and Depth

Sea surface density is derived from satellite SSS and SST. Using wind and air density from ERA5 (or wind from saildrones and air density from ERA5), wind stress (τ) is estimated as:

$$\tau_u = C_D \cdot |U_{ERA5}| \cdot U_{ERA5} \cdot \rho_{ERA5} \tag{2}$$

$$\tau_v = C_D \cdot |V_{ERA5}| \cdot V_{ERA5} \cdot \rho_{ERA5}, \tag{3}$$

with C_D the surface drag coefficient calculated following Foreman and Emeis (2010), $C_D = \frac{(0.051 \cdot WS_{ERA5} - 0.14)^2}{WS_{ERA5}^2}$ and $WS_{ERA5} = \sqrt{U_{ERA5}^2 + V_{ERA5}^2}$. In the range of WS_{ERA5} from 1 to 20 m s^{-1}, CD ranges from 0 to 0.008. Combining wind stress and sea surface density we estimate the horizontal Ekman transport in ice-free regions as (Gill & Adrian, 1982; Tarasenko et al., 2021):

$$T_{u_{ekm}} = \frac{\tau_v}{\rho \cdot f} \tag{4}$$

$$T_{v_{ekm}} = -\frac{\tau_u}{\rho \cdot f}, \tag{5}$$

where f is the Coriolis parameter.

Using shear derived from ADCP (Section 2.1.2) it is possible to estimate the depth scale of the Ekman current spiral, the Ekman depth (D_{ekm}). Following Lenn and Chereksin (2009), and Schudlich and Price (1998), we express D_{ekm} as:

$$D_{ekm} = \sqrt{\frac{2\rho K}{|f|}} \qquad (6)$$

With

$$\rho K = \frac{\overline{\tau}}{\text{Shear}}, \qquad (7)$$

where $\overline{\tau}$ is the magnitude of the wind stress and K the turbulent diffusivity. In this study, we compute K using a linear fit between the shear and $\overline{\tau}$.

3. Validation of Satellite SSS Along the Saildrone Trajectories

Figure 1 illustrates the saildrone trajectories through the Bering Strait, the Chukchi Sea, and the Beaufort Sea, following the sea ice retreat during summer 2019. The two saildrones start very close to each other (at less than 5 km separation) but then take different paths in the Beaufort Sea. At the end of the entire time series considered in the study, the distance between the saildrones exceeds 380 km. The SSS and SST from the two saildrones' time series illustrate the very high variability in this area, with SSS values varying between 25 and 32.5 pss and SST values between −1 and 10°C, over 3 months (Figures 2 and 3a–3d).

We compare saildrone and satellite measurements through the analysis of six specific time periods corresponding to different situations, indicated on Figure 1. In the following, "period *X-Y*" refer to the time span separating event *X* and event *Y*. The two first events correspond to two freshening events briefly detected by the saildrones in the vicinity of sea ice (Event 1 on 2019/06/19 and Event 2 on 2019/07/05). At the end of July, the focus is on a large Chukchi Sea MWL (Event 3 on 2019/07/25), corresponding to the end of the crossing of a MWL by the saildrones. In August, the proximity of saildrones with the sea ice edge in the Beaufort Sea is analyzed (Event 4 on 2019/08/08). Finally, the two saildrones follow different pathways between the middle of August (Event 5 on 2019/08/15) at the exit of the Beaufort Sea MWL and early September (Event 6 on 2019/09/05), when S1036 records high frequency variability.

In the Bering Strait, the saildrones crossed relatively salty PW (Figure 2a). During this period (prior to Event 1), many satellite SSS values are filtered (Figures 3a and 3b), consistent with the proximity of the saildrones to sea ice and the coastline. Consequently, the satellite weekly SSS retrieval uncertainties remain high (between 0.4 and 0.7 pss), explaining the high spread of the differences between the satellite and saildrone SSS. The absolute difference between saildrones and SMOS + SMAP SSS is the largest observed, exceeding 2.5 pss (Figures 3a and 3b). During the journey of the two saildrones northward, S1037 recorded a large decrease in SSS and SST, from more than 30–26 pss and from 5 to −1°C (Event 1). The signature of this event is much weaker on S1036 records and poorly captured by satellite SSS and SST measurements (Figures 3a and 3b). The SIC map indicates the presence of a thin ice filament of low concentration (Figure 4a). S1037 was closer to this filament and probably crosses an MWL. After this event, during period 1–2, both SSS and SST quickly increase and reach values characteristic of PW. The STDD during period 1–2 is the highest of the other periods. It reaches 0.92 pss between SMOS + SMAP SSS and S1036 (STDD$_{S1036}$) and 1.01 pss between SMOS + SMAP SSS and S1037 (STDD$_{S1037}$).

Event 2 corresponds to another short event of SSS and SST decrease (Figures 3a–3d) close to the sea ice edge (Figure 4b). This time, both saildrones measured these decreases, although the freshening captured by S1037 (more than 2 pss) was larger than captured by S1036 (less than 1 pss). This event was not detected by satellite SSS, while satellite SST shows a decrease, albeit with a weaker magnitude. WS (Figures 3e and 3f) and surface currents (Figures 3g and 3h) were very low during this event (close to 0 m s^{-1}) but they follow and precede larger WS and surface currents (up to more than 10 m s^{-1} for WS and more 0.4 m s^{-1} for the zonal component of the surface current) recorded by the saildrones.
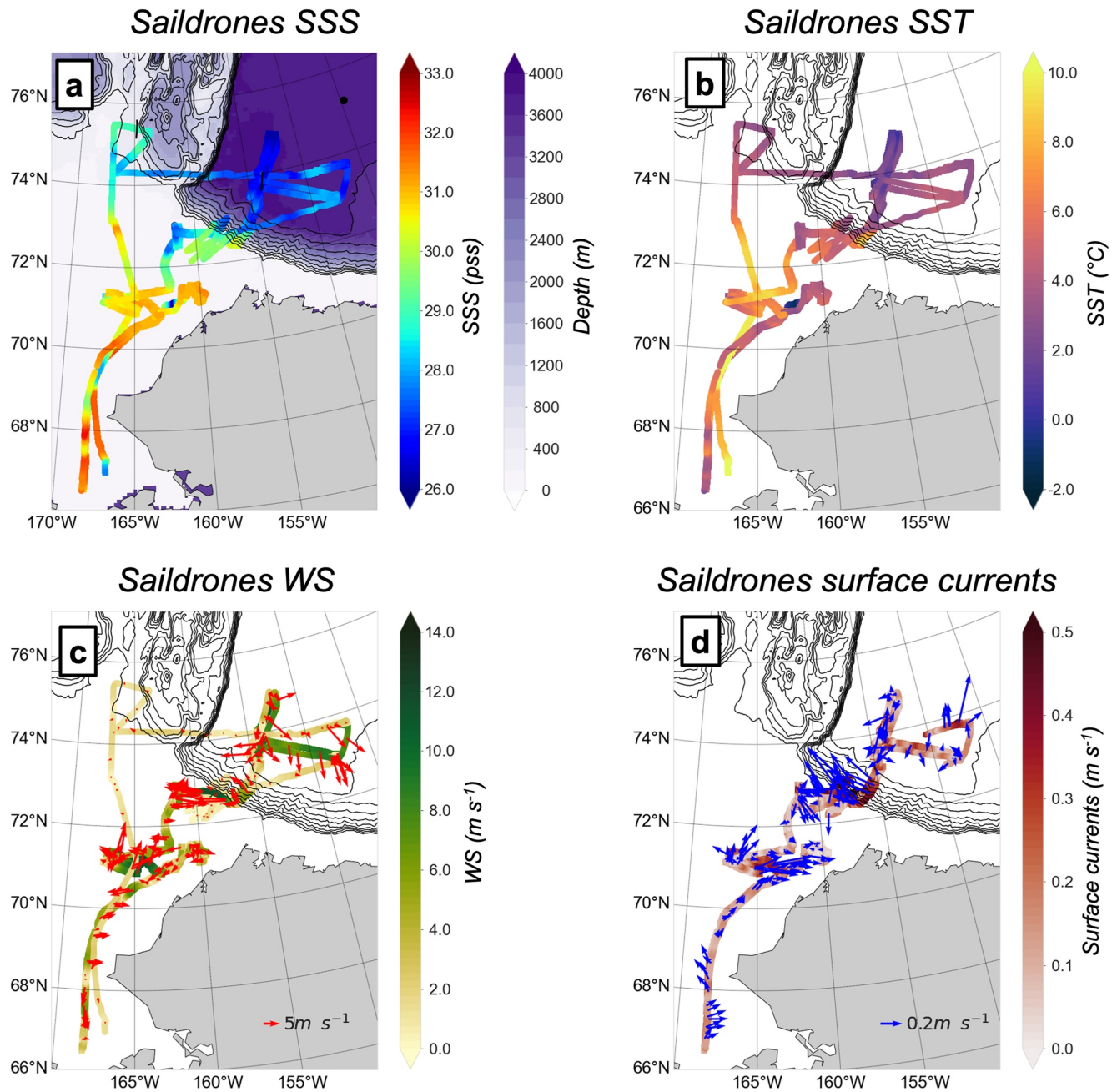
Figure 2. Measurements from saildrones: (a) Sea Surface Salinity, background colors indicate the bathymetry; (b) sea surface temperature; (c) Wind Speed (WS), oriented arrow for direction, scaled with WS magnitude; (d) surface currents (oriented arrow for direction, scaled with currents magnitude) in the Bering Strait, Chukchi and Beaufort Sea from June to September 2019.

During period 2–3, SSS and SST decrease for almost 10 days followed by an increase over 10 days. Event 3 is recorded at the end of the crossing of the largest MWL observed by the saildrones (Figures 3a and 3b). Figure 4c illustrates well the area occupied by the MWL just crossed by the two saildrones. At the end of period 2–3, SSS and SST increase is associated with an increase in WS that exceeds 10 m s^{-1}. The amplitude of the MWL is captured very well by satellite estimates of SSS and SST (Figures 3a–3d). During this period, SMOS + SMAP SSS STDD does not exceed 0.52 pss for STDD$_{S1036}$ and 0.73 pss for STDD$_{S1037}$. This MWL is described in more detail in Section 4.
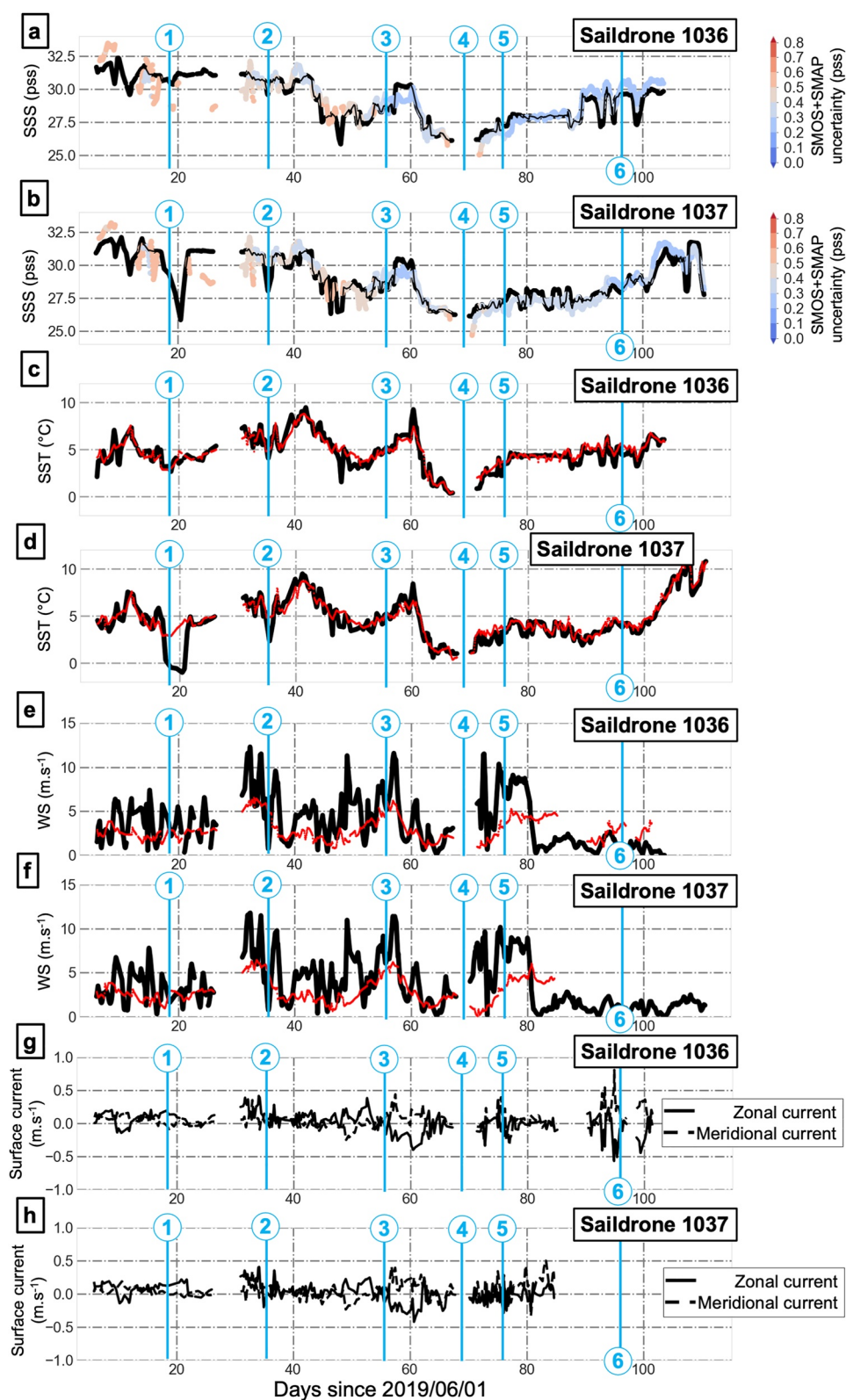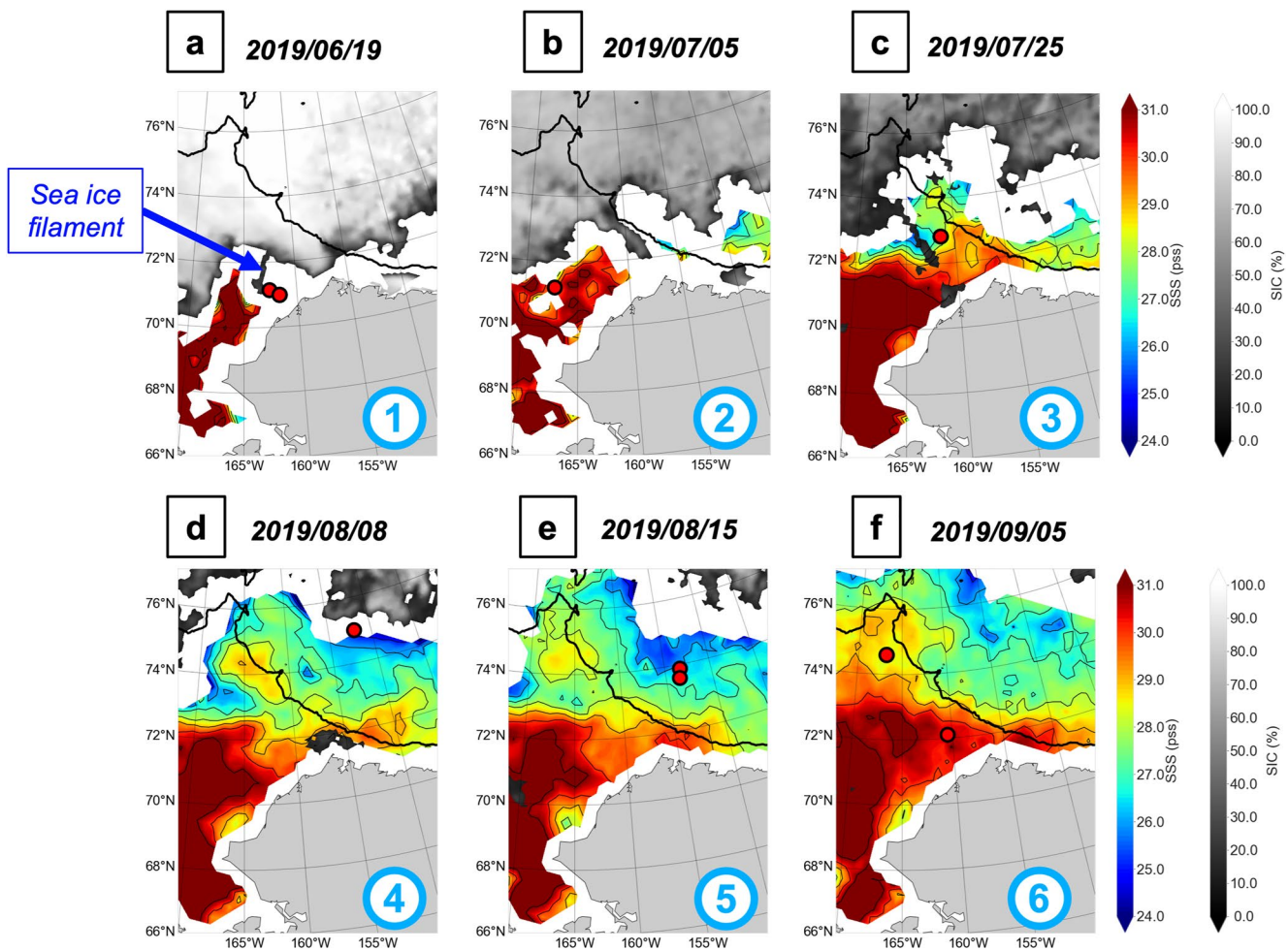
Figure 3.

Figure 4. SMOS + SMAP SSS and OSI-SAF SIC for (a) 2019/06/19, (b) 2019/07/05, (c) 2019/07/25, (d) 2019/08/08, (e) for 2019/08/15, (f) 2019/09/05. Black bold line indicates 500 m isobath. Red dots indicate the saildrone positions on that day. See similar maps of SMOS and SMAP SSS considered independently in Figures S5 and S6 in Supporting Information S1. The blue numbers indicate the various stages described in the text.

Once they exited the MWL, the saildrones crossed surface water with characteristics corresponding to PW (early in period 2–3, SSS slightly above 30 pss). After the MWL, they entered the Beaufort Sea, where they record an inversion of surface currents (Figures 3g and 3h), associated with the crossing of the Chukchi slope current.

Up to Event 4, before the saildrones reached the sea ice edge and headed back south (after 70 days), SST and SSS strongly decrease. The return to lower latitudes (period 4–5) was then associated with an increase in SSS and SST. This evolution was well observed by satellite SSS ($STDD_{S1036}$ = 0.60 pss and $STDD_{S1037}$ = 0.54 pss) and SST. Nevertheless, close to the sea ice edge (and despite the sea ice filtering applied to the satellite product), the SMOS + SMAP product underestimates SSS by up to 1.5 pss in the worst case (around day 70; Figures 3a and 3b).

During period 5–6, the two saildrones headed in different directions. S1036 headed straight back southward to the Chukchi Sea, while S1037 traveled to the west. During that period, SST and SSS gradients were well reproduced by satellite measurements.

Figure 3. (a) S1036 sea surface salinity (SSS) measurement time series (black) and SMOS + SMAP collocated SSS in color (color for SSS uncertainty); (b) S1037 SSS measurement time series (black) and SMOS + SMAP collocated SSS in color (color for SSS uncertainty); (c) S1036 sea surface temperature (SST) measurement time series (black) and Remote Sensing Systems (RSS) collocated SST (red); (d) S1037 SST measurement time series (black) and RSS collocated SST (red); (e) S1036 wind speed (WS) measurement time series (black) and ERA5 collocated WS (red); (f) S1037 WS measurement time series (black) and ERA5 collocated WS (red); (g) S1036 surface currents measurements time series; (h) S1037 surface currents measurements time series. The blue numbers indicate the various periods described in the text. See similar time series of Soil Moisture and Ocean Salinity and SMAP SSS considered independently in Figure S4 in Supporting Information S1.
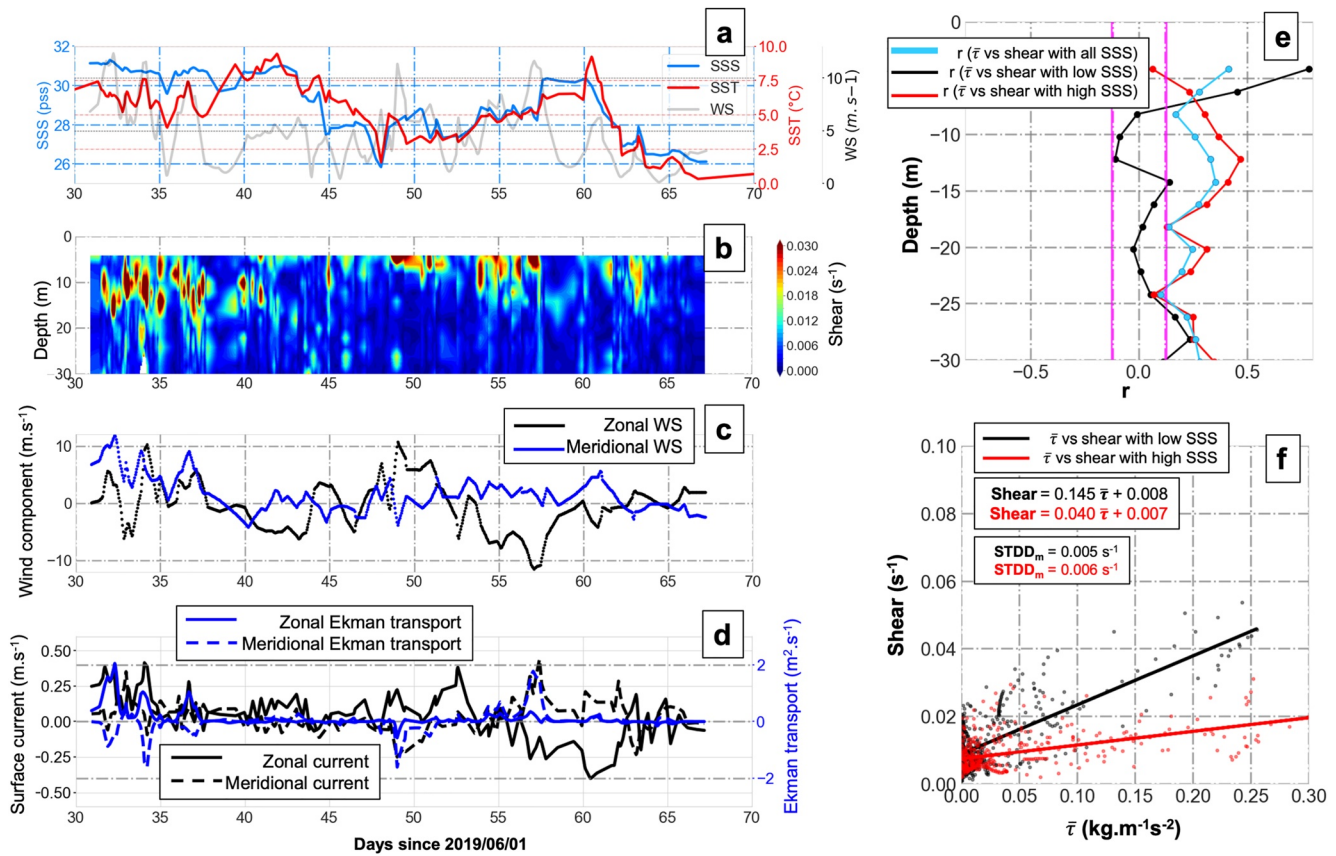
Figure 5. S1036 measurements between day 30 and day 70 (since 2019/06/01) of (a) sea surface salinity (SSS) (blue), SST (red) and wind speed (WS) (gray); (b) vertical shear between 0 and 30 m depth computed from current profiles; (c) zonal (black) and meridional (blue) wind component; (d) zonal and meridional component of surface current (black) and estimated Ekman transport (blue); (e) correlation between WS and shear as a function depth for all SSS (blue), low SSS (under 29 pss, black) and high SSS (above 29 SSS, red) magenta line correspond to minimum significative correlation value for the significance level $\alpha = 0.01$; (f) scatterplot between shear and $\bar{\tau}$ for low SSS (under 29 pss, black) and high SSS (above 29 SSS, red), full lines correspond to linear fit. STDDm corresponds to standard deviation of difference between modelized and true values.

Finally, both saildrones were back in the Chukchi Sea at the end of period 5–6. In the eastern part, S1036 crossed PW while, further north, S1037 was in an area with relatively low SSS, presumably caused by sea ice melt (Figures 3b and 4f). For S1036, Event 6 is an illustration of high frequency changes (in SSS and SST) which were recorded consistently with S1036 and satellites.

Over the entire time series, the STDD of SMOS + SMAP SSS with the two saildrones is 0.75 pss. The large variability observed during the saildrones' journeys and the relatively low STDD resulted in a high correlation level between SMOS + SMAP SSS and S1036 ($r = 0.88$) and S1037 ($r = 0.90$).

4. A Large Persistent Meltwater Lens in the Chukchi Sea

Between days 43 and 60, both saildrones monitored a large MWL (Figures 3a and 3b). This MWL was characterized by a large SSS decrease associated with a strong SST decrease (Figure 5a), with low values persisting for more than 2 weeks. Saildrone SSS and SST values fell to 26 pss and 2°C respectively (corresponding to a decrease of 5 pss and 6°C compared to the values measured by the saildrone before entering the MWL). Figures 5a and 5c show the large variability in WS measured by S1036 between day 30 and day 70. Wind stress transfers momentum to the sea surface, generating a vertical current shear (Figure 5b). In the general case (all SSS considered), correlation between WS and vertical shear reaches values close to 0.5 for the shallowest level and decrease with depth (Figure 5e). As expected, S1036 shows an increase in vertical shear intensity when WS increases. Between days 37 and 47, and between days 57 and 70, WS was relatively low and no significant vertical shear was generated, in contrast to periods between days 30 and 37 and between days 47 and 57. For periods
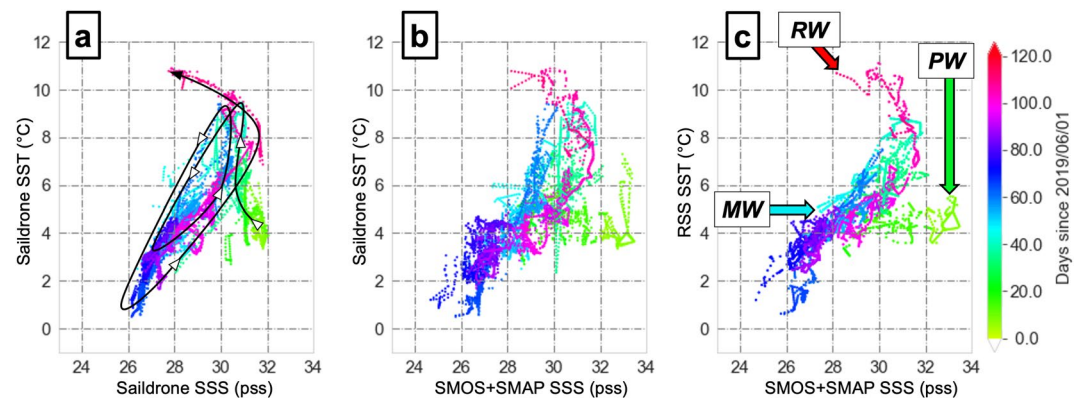
Figure 6. T/S diagrams from (a) in situ S1037 sea surface temperature (SST) and sea surface salinity (SSS), (b) in situ S1037 SST and SMOS + SMAP SSS collocated with S1037 trajectory, and (c) Remote Sensing Systems SST and SMOS + SMAP SSS collocated with S1037 trajectory. On (a) the arrows show the saildrone trajectory. Water masses indicated on panel (c) are Meltwater, Riverine Water and Pacific Water.

with a significant vertical shear, we compare each component of the shallowest S1036 current measurement to the respective components of Ekman transport derived from WS measured by the same saildrone. Figures 5c and 5d show that the variability of the currents was coherent with Ekman transport during large WS events, at the beginning of the period (days 30–37) and at the end of the period (day 47–57 when zonal transport is associated with large meridional WS). For WS larger than 3 m s^{-1} (40% of the time between day 30 and 70), the correlation between surface current velocity and Ekman transport magnitude reaches 0.43. However, there is an exception for the zonal current during the period between day 52 and day 62 that was dominated by the slope current between the Chukchi and the Beaufort Sea. Excluding this event, the correlation between the surface current velocity and Ekman transport magnitude reaches 0.78 for WS above 3 m s^{-1} (28% of the time).

Between day 30 and day 70, the vertical shear showed a variable penetration of momentum associated with wind stress (Figure 5b). We choose to separate relatively high and relatively low SSS by a 29 pss threshold. This threshold corresponds to the lowest SSS value observed by saildrones before they cross MWL. When SSS is relatively high, wind events are associated with a vertical extent of current shear due to momentum transfer from wind stress. Correlation between $\overline{\tau}$ and vertical shear increases with depth with a maximum value between 10 and 15 m. Correlation decreases to 0 between 20 and 25 m (Figure 5e). The penetration of the wind effect was limited when S1036 crosses the MWL and low SSS areas (under 29 pss). There, the wind-influenced layer was constrained to the first 10 m. Correlation between $\overline{\tau}$ and the vertical shear decreases with depth and reaches 0 roughly at 10 m depth (Figure 5e).

We used the scatterplot between $\overline{\tau}$ and the shear (Figure 5f) and Equation 7 to compute the averaged K value in the two situations. As we considered the layer under the influence of wind, the shear value corresponds to the averaged shear between the surface and the first depth reaching a non-significative correlation between shear and $\overline{\tau}$, that is, 8.2 m under 29 pss and 18.2 m above 29 pss (Figure 5e). We find a K value of 0.0065 ± 0.0002 m^2 s^{-1} under 29 pss and of 0.0244 ± 0.0043 m^2 s^{-1} above 29 pss respectively. We determine Dekm in the two scenarios using Equation 6. We find an average Ekman depth ranging from 9.7 ± 0.2 m (under 29 pss) to 18.8 ± 1.6 m (above 29 pss). These results confirm that low SSS suppressed the deepening of the Ekman layer.

5. Sea Surface Variability Following Sea Ice Retreat Over the Chukchi and the Beaufort Seas

During their journey, both saildrones crossed various water masses at the sea surface. Figure 6 shows their signature in T/S diagrams, comparing in situ and satellite observations. Satellite estimates reproduce well the variability of surface water masses. The following water masses can be identified from both the saildrone and satellite measurements: (a) low SSS and low SST meltwater associated with sea ice melt observed in the Beaufort and Chukchi seas; (b) relatively warm and fresh RW; (c) relatively cold and salty PW.

Given our demonstration of the ability of SMOS + SMAP SSS to realistically capture SSS synoptic variability and to monitor different surface water masses, we make use of these measurements to examine the spatial and temporal context leading to the appearance of the MWL. To do so, we focus on Hovmöller diagrams of SSS, SST and Ekman transport (from satellites for SSS and SST, and ERA5 reanalysis for WS and the associated Ekman transport) along the two transects shown in Figure 1. The first Hovmöller diagram is representative of the surface conditions in the Chukchi Sea (Figure 7) and the second one of the Beaufort Sea (Figure 8).

The main signal in SSS visible in the first transect across the Chukchi Sea corresponds to the low SSS signal associated with the MWL visible between 72° and 75°N and between days 40 and 70 (Figure 7a). The period covered by the Hovmöller diagram starts in early June, when the full transect was ice-covered. As sea ice retreated during June, satellite SSS measurements revealed the presence of saline surface water along the transect, albeit close to the sea ice edge where SSS and SST variability was larger and dominated by episodic low SSS events or a small MWL (Figure 7a). For example, on day 22, colder and fresher sea surface close to the sea ice edge is present for a short period of time, which follows a period centered on day 20 characterized by the presence of salty and warm water (Figures 7a and 7b).

At the end of June and in early July, the Ekman transport was mainly oriented eastward (Figures 7c and 7d) and could potentially drive part of the sea ice retreat by advecting sea ice in the same direction or by bringing warm water to the sea ice edge. As sea ice retreated, a large MWL became visible. From day 40 onward (mid-July), the large MWL described in Section 4 started to occupy the Chukchi Sea for a period longer than a month. The contrast of the surface properties found within the MWL and in the surrounding region was also accentuated by the increase in SSS north of it that occurred in August (day 61). Between the middle and the end of August, an increase in Ekman transport toward the southwest (due to an increase of WS) was associated with the disappearance of the MWL, followed afterward by a decrease in SST (day 85).

Along the second transect in the Beaufort Sea (Figure 8), the sea ice only retreated in July, so that satellite SSS and SST monitoring there starts later than in the Chukchi Sea. Nevertheless, this transect presents some similarities with Transect 1. In July (around day 30), low SSS appears close to the sea ice edge. By the middle of July, a few days after the event that brought warm water under the influence of Ekman transport in the Chukchi Sea, warm and salty water was also visible in the Beaufort Sea (albeit associated with smaller increases in SSS and SST). Similar to the Chukchi Sea, this anomalous advection was followed by a large sea ice retreat. In contrast to the Chukchi Sea, the northward retreat of sea ice resulted in the appearance of a water mass between 73° and 75°N with relatively high SSS and low SST. In August (starting on day 61), the SSS contrast across the transect was strongly enhanced, due to the decrease of SSS north of 73°N and its increase south of 73°N.

In September (starting on day 92), the surface water masses became warm and salty south of 72°N, likely under the influence of the advection of PW from the Chukchi Sea, although the Ekman transport did not exhibit any significant increase.

6. Discussion and Conclusion

During summer 2019, two saildrones explored the Chukchi and Beaufort seas, allowing for monitoring the large SSS and SST variability found in this region. They crossed persistent surface water masses such as RW along the Alaskan coast and PW advected into the Chukchi Sea. Additionally, they also crossed regions with short-lived low SSS areas, such as MWLs. The different observed MWLs were associated with different freshening amplitudes (from a few tenths of a pss to 5 pss) and were found at different distances from the sea ice edge. Measurements from the two saildrones revealed a large variability in SSS and SST in the vicinity of MWLs with SSS values between 25 and 32.5 pss and SST between −1 and 10°C.

The largest MWL captured during the campaign was observed in July and August, far away from the sea ice edge, and was associated with low SST (the decrease in SSS reaches 5 pss and the decrease in SST reaches 6°C). Saildrone measurements of ocean currents and wind further revealed that, in the presence of low SSS associated with the MWL, the increase in vertical shear driven by an increase in WS remains trapped close to the surface (down to 10 m). This is likely due to an increase in stratification in the MWL resulting from the SSS decrease. This suggests that the presence of MWL, and their associated stratification of surface water properties, have the potential to modulate the ocean response to the winds, and the air-sea momentum transfer.
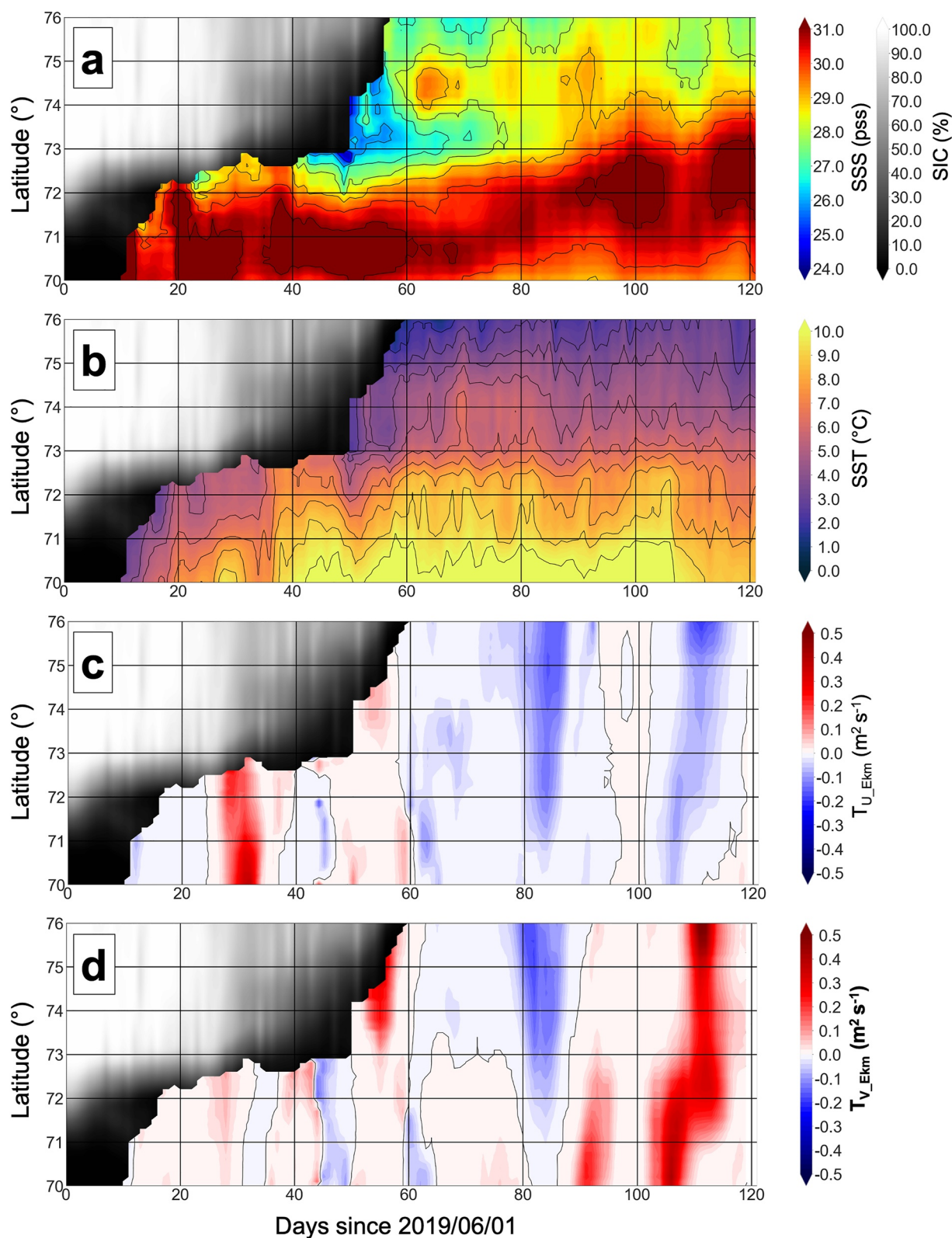
Figure 7. Hovmöller diagrams along Transect 1 in the Chukchi Sea (Figure 1; between 70° and 76°N at 165°W): (a) SMOS + SMAP SSS; (b) RSS SST; (c) zonal component of Ekman transport; (d) meridional component of Ekman transport.
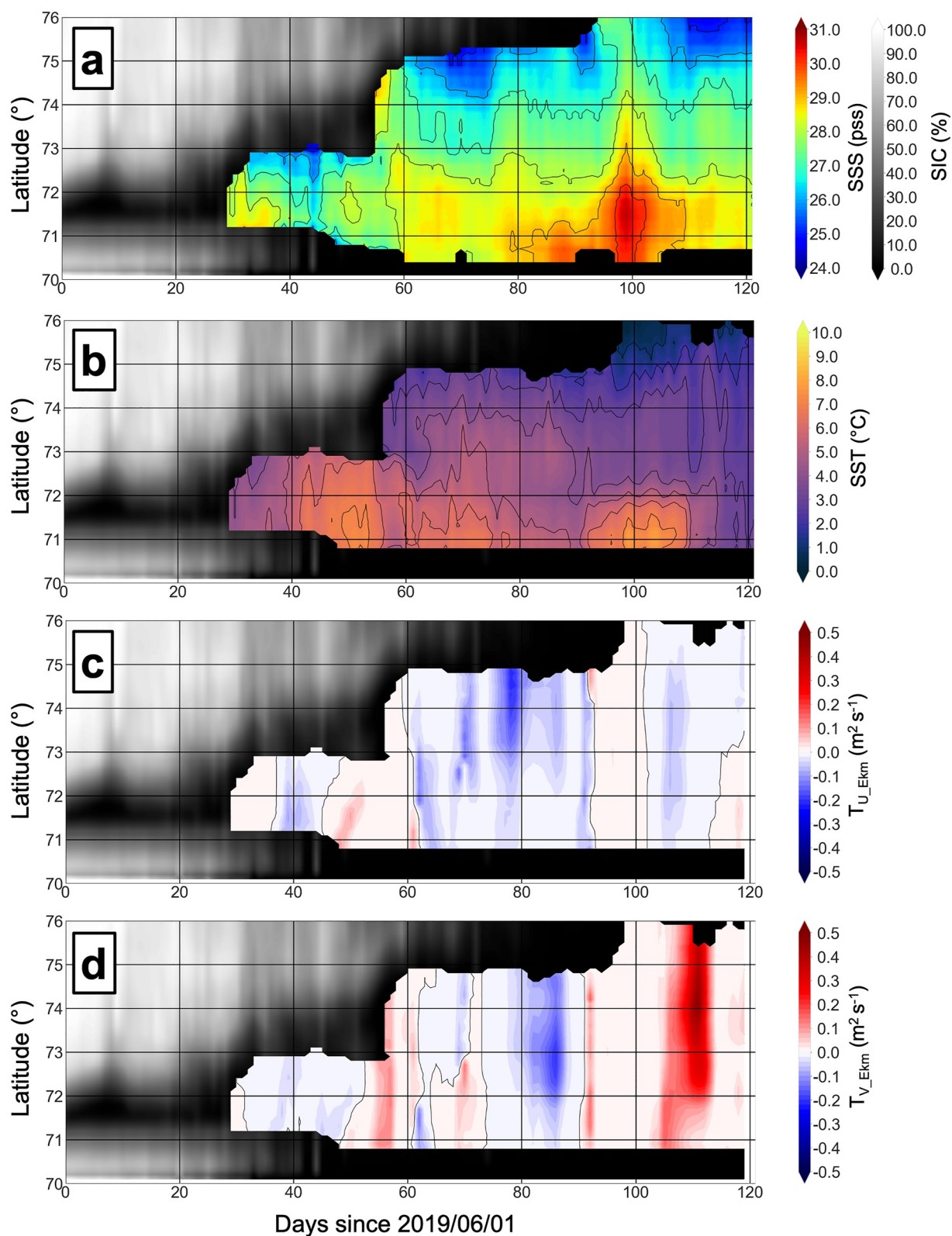
Figure 8. Hovmöller diagrams along Transect 2 in the Beaufort Sea (Figure 1; between 70° and 76°N at 150°W): (a) SMOS + SMAP SSS; (b) RSS SST; (c) zonal component of Ekman transport; (d) meridional component of Ekman transport.

To provide some broader spatial and temporal context to the local in situ observations gathered by the saildrones, we examined satellite observations of SSS and SST. Despite the large uncertainties associated with satellite SSS estimates over the Arctic Ocean, it has previously been shown to provide valuable information regarding the water masses evolution in ice free regions (Tarasenko et al., 2021).

We found that SSS retrieved from the combination of SMOS and SMAP measurements captured well the variability in SSS measured by the saildrones. Associated with RSS SST estimates, we demonstrated that the satellite products provide consistent T/S diagrams representing the different water masses found at the surface of the region considered, as well as the strong decrease in SST and SSS captured by the saildrones.

Considering the temporal evolution of properties of the surface water masses following the sea ice retreat, we found that the sea ice melt over the Chukchi Sea resulted in a large and long lasting MWL. Over the Beaufort Sea, the satellite measurements revealed the presence of lower SSS than over the Chukchi Sea, due to the overlapping of MWL over the Beaufort Gyre. Values of SSS below 28 pss are not unusual in the Beaufort Sea, in contrast to the values measured in the Chukchi Sea. Additionally, several MWLs were captured, as seen by SSS decreases. In line with the study of Dewey et al. (2017), we found that the intensity of the freshening decreases as the distance from the sea ice edge increases. Furthermore, we found that the MWL can be associated with two different types of dynamics: MWL evolution follows the meridional sea ice retreat over the Beaufort Sea while, in the Chukchi Sea, a large persisting MWL is generated by the advection of a sea ice filament. However, regardless of the type of MWL, regions of low SSS induced by sea ice melting occupied a significant part of the Beaufort and the Chukchi seas during summer 2019.

Further investigations are needed to fully understand the roles of mixing and advection in the temporal evolution of the freshwater lenses, their occurrence and persistence, and interactions with ocean dynamics and biogeochemistry. Nonetheless, the combined use of satellite-measured SSS and SST and atmospheric reanalysis will be key to monitoring the sea surface characteristics during the melting period. The ability of L-band radiometric SSS to detect sea ice melt effects is particularly encouraging in the changing Arctic Ocean, but additional improvements could also be done regarding the strategy used for sea ice contamination mitigation. Here we chose to remove all measurements suspected of being influenced by sea ice to ensure a reduced uncertainty. Recent studies, however, suggest that SSS could be retrieved in pixels partially covered by sea ice (Tang et al., 2021). Nevertheless, increasing proportion of areas covered by seasonal sea ice, and thus free of ice during summer, enhances the satellites' ability to monitor Arctic surface water properties. The synergy between satellite and in situ measurements is also fundamental to understand the full dynamics of the MWL and, in particular the influence of vertical processes for their evolution.

Overall, our study highlights the need for improvement in SSS retrievals from future satellite missions. A mission such as the proposed SMOS-HR project (Rodríguez-Fernández et al., 2019), that aims to estimate SSS with L-band interferometric radiometer measurements with a 10-km resolution, would allow for better identification of measurements contaminated by sea ice, and detection of thin sea ice filaments or sea ice patches extracted by ocean currents from these filaments. An improved resolution would also allow for a retrieval of SSS closer to the sea ice edge and thus to more accurately capture the properties of MWLs.

Data Availability Statement

We benefited from numerous data sets made freely available that are listed here: Saildrone Arctic field campaign surface measurements for NOPP-MISST project (https://podaac-tools.jpl.nasa.gov/drive/files/allData/insitu/L2/saildrone/Arctic), JPL SMAP SSS (https://podaac-tools.jpl.nasa.gov/drive/files/SalinityDensity/smap/L3/JPL/V4.3/8day_running) provided by Physical Oceanography Distributed Active Archive Center, OSI-SAF SIC provided by Norwegian Meteorological Institute (https://thredds.met.no/thredds/osisaf/osisaf_seaiceconc.html), RSS SST provided by Remote Sensing System (https://www.remss.com/measurements/sea-surface-temperature/) and ERA5 WS and air density provided by the Copernicus Climate Change Service (https://cds.climate.copernicus.eu/cdsapp%23%21/dataset/reanalysis%2Dera5%2Dsingle%2Dlevels%3Ftab%3Doverview).

References

Boutin, J., Vergely, J. L., Dinnat, E. P., Waldteufel, P., d'Amico, F., Reul, N., et al. (2020). Correcting sea surface temperature spurious effects in salinity retrieved from spaceborne L-band radiometer measurements. *IEEE Transactions on Geoscience and Remote Sensing*, *59*(9), 7256–7269. https://doi.org/10.1109/TGRS.2020.3030488

Carmack, E. C., Yamamoto-Kawai, M., Haine, T. W. N., Bacon, S., Bluhm, B. A., Lique, C., et al. (2016). Freshwater and its role in the Arctic marine system: Sources, disposition, storage, export, and physical and biogeochemical consequences in the Arctic and global oceans. *Journal of Geophysical Research: Biogeosciences*, *121*(3), 675–717. https://doi.org/10.1002/2015JG003140

Coachman, L. K., Aagaard, K., & Tripp, R. B. (1975). *Bering Strait: The regional physical oceanography*. University of Washington Press.

Danielson, S. L., Ahkinga, O., Ashjian, C., Basyuk, E., Cooper, L. W., Eisner, L., et al. (2020). Manifestation and consequences of warming and altered heat fluxes over the Bering and Chukchi Sea continental shelves. *Deep Sea Research Part II: Topical Studies in Oceanography*, *177*, 104781. https://doi.org/10.1016/j.dsr2.2020.104781

Dewey, S. R., Morison, J. H., & Zhang, J. (2017). An edge-referenced surface fresh layer in the Beaufort Sea seasonal ice zone. *Journal of Physical Oceanography*, *47*(5), 1125–1144. https://doi.org/10.1175/JPO-D-16-0158.1

Font, J., Camps, A., Borges, A., Martin-Neira, M., Boutin, J., Reul, N., et al. (2010). SMOS: The challenging sea surface salinity measurement from space. *Proceedings of the IEEE*, *98*(5), 649–665. https://doi.org/10.1109/jproc.2009.2033096

Fore, A., Yueh, S., Tang, W., & Hayashi, A. (2019). SMAP salinity and wind speed data user's guide.

Foreman, R. J., & Emeis, S. (2010). Revisiting the definition of the drag coefficient in the marine atmospheric boundary layer. *Journal of Physical Oceanography*, *40*(10), 2325–2332. https://doi.org/10.1175/2010JPO4420.1

Gaillard, F., Reynaud, T., Thierry, V., Kolodziejczyk, N., & Von Schuckmann, K. (2016). In situ–based reanalysis of the global ocean temperature and salinity with ISAS: Variability of the heat content and steric height. *Journal of Climate*, *29*(4), 1305–1323. https://doi.org/10.1175/JCLI-D-15-0028.1

Gentemann, C. L., Scott, J. P., Mazzini, P. L. F., Pianca, C., Akella, S., Minnett, P. J., et al. (2020). Saildrone: Adaptively sampling the marine environment (2020). *Bulletin of the American Meterological Society*, *101*(6), E744–E762. https://doi.org/10.1175/BAMS-D-19-0015.1

Gill, A. E., & Adrian, E. (1982). *Atmosphere-ocean dynamics* (Vol. 30). Academic Press.

Hersbach, H., Bell, B., Berrisford, P., Hirahara, S., Horányi, A., Muñoz-Sabater, J., et al. (2020). The ERA5 global reanalysis. *Quarterly Journal of the Royal Meteorological Society*, *146*(730), 1999–2049. https://doi.org/10.1002/qj.3803

Kerr, Y. H., Waldteufel, P., Wigneron, J. P., Delwart, S., Cabot, F., Boutin, J., et al. (2010). The SMOS mission: New tool for monitoring key elements of the global water cycle. *Proceedings of the IEEE*, *98*(5), 666–687. https://doi.org/10.1109/JPROC.2010.2043032

Kolodziejczyk, N., Hamon, M., Boutin, J., Vergely, J. L., Reverdin, G., Supply, A., & Reul, N. (2021). Objective analysis of SMOS and SMAP sea surface salinity to reduce large-scale and time-dependent biases from low to high latitudes. *Journal of Atmospheric and Oceanic Technology*, *38*(3), 405–421. https://doi.org/10.1175/JTECH-D-20-0093.1

Lenn, Y., & Chereskin, T. K. (2009). Observations of Ekman currents in the Southern Ocean. *Journal of Physical Oceanography*, *39*(3), 768–779. https://doi.org/10.1175/2008JPO3943.1

Liu, J., Scott, K. A., Gawish, A., & Fieguth, P. (2016). Automatic detection of the ice edge in SAR imagery using curvelet transform and active contour. *Remote Sensing*, *8*(6), 480. https://doi.org/10.3390/rs8060480

MacKinnon, J. A., Simmons, H. L., Hargrove, J., Thomson, J., Peacock, T., Alford, M. H., et al. (2021). A warm jet in a cold ocean. *Nature Communications*, *12*(1), 1–12. https://doi.org/10.1038/s41467-021-22505-5

Martínez, J., Gabarró, C., Turiel, A., González-Gambau, V., Umbert, M., Hoareau, N., et al. (2022). Improved BEC SMOS Arctic Sea surface salinity product v3.1. *Earth System Science Data*, *14*(1), 307–323. https://doi.org/10.5194/essd-14-307-2022

Matsuoka, A., Babin, M., & Devred, E. C. (2016). A new algorithm for discriminating water sources from space: A case study for the southern Beaufort Sea using MODIS ocean color and SMOS salinity data. *Remote Sensing of Environment*, *184*, 124–138. https://doi.org/10.1016/j.rse.2016.05.006

Meissner, T., Wentz, F. J., Scott, J., & Vazquez-Cuervo, J. (2016). Sensitivity of ocean surface salinity measurements from Spaceborne L-band radiometers to Ancillary Sea surface temperature. *IEEE Transactions on Geoscience and Remote Sensing*, *54*(12), 7105–7111. https://doi.org/10.1109/TGRS.2016.2596100

Mordy, C. W., Cokelet, E. D., De Robertis, A., Jenkins, R., Kuhn, C. E., Lawrence- Slavas, N., et al. (2017). Advances in ecosystem research: Saildrone surveys of oceanography, fish, and marine mammals in the Bering Sea. *Oceanography*, *30*(2), 113–115. https://doi.org/10.5670/oceanog.2017.230

Olmedo, E., Gabarró, C., González-Gambau, V., Martínez, J., Ballabrera-Poy, J., Turiel, A., et al. (2018). Seven years of SMOS Sea surface salinity at high latitudes: Variability in Arctic and sub-Arctic regions. *Remote Sensing*, *10*(11), 1772. https://doi.org/10.3390/rs10111772

Perrot, X., Boutin, J., Vergely, J. L., Rouffi, F., Martin, A., Guimbard, S., et al. (2021). CCI+SSS, A new SMOS L2 reprocessing reduces errors on sea surface salinity time series. In *2021 IEEE international geoscience and remote sensing symposium IGARSS* (pp. 7457–7460). https://doi.org/10.1109/IGARSS47720.2021.9554451

Piepmeier, J. R., Focardi, P., Horgan, K. A., Knuble, J., Ehsan, N., Lucey, J., et al. (2017). SMAP L-band microwave radiometer: Instrument design and first year on orbit. *IEEE Transactions on Geoscience and Remote Sensing*, *55*(4), 1954–1966. https://doi.org/10.1109/TGRS.2016.2631978

Polyakov, I. V., Alkire, M., Bluhm, B., Brown, K., Carmack, E. C., Chierici, M., et al. (2020). Borealization of the Arctic Ocean in response to anomalous advection from sub-Arctic seas. https://doi.org/10.3389/fmars.2020.00491

Reul, N., Grodsky, S. A., Arias, M., Boutin, J., Catany, R., Chapron, B., et al. (2020). Sea surface salinity estimates from spaceborne L-band radiometers: An overview of the first decade of observation (2010–2019). *Remote Sensing of Environment*, *242*, 111769. https://doi.org/10.1016/j.rse.2020.111769

Rodrıguez-Fernández Nemesio, J., Anterrieu, E., Rouge, B., Boutin, J., Picard, G., Pellarin, T., et al. (2019). SMOS-HR: A high-resolution L-band passive radiometer for Earth science and applications. In *IEEE international geoscience and remote sensing symposium 2019* (pp. 8392–8395). https://doi.org/10.1109/IGARSS.2019.8897815

Schudlich, R. R., & Price, J. F. (1998). Observations of seasonal variation in the Ekman Layer. *Journal of Physical Oceanography*, *28*(6), 1187–1204. https://doi.org/10.1175/1520-0485(1998)0282.0.CO;2

Steele, M., Ermold, W., & Zhang, J. (2011). Modeling the formation and fate of the near-surface temperature maximum in the Canadian Basin of the Arctic Ocean. *Journal of Geophysical Research*, *116*(C11). https://doi.org/10.1029/2010JC006803

Steele, M., Morison, J., Ermold, W., Rigor, I., Ortmeyer, M., & Shimada, K. (2004). Circulation of summer Pacific halocline water in the Arctic Ocean. *Journal of Geophysical Research*, *109*(C2), C02027. https://doi.org/10.1029/2003JC002009

Supply, A., Boutin, J., Kolodziejczyk, N., Reverdin, G., Lique, C., Vergely, J.-L., & Perrot, X. (2022). SMOS and SMAP combined SSS L3 maps over the Chukchi and the Beaufort seas during summer 2019. *SEANOE*. https://doi.org/10.17882/87747

Supply, A., Boutin, J., Vergely, J.-L., Kolodziejczyk, N., Reverdin, G., Reul, N., & Tarasenko, A. (2020a). New insights into SMOS sea surface salinity retrievals in the Arctic Ocean. *Remote Sensing of Environment*, *249*, 112027. https://doi.org/10.1016/j.rse.2020.112027

Supply, A., Boutin, J., Vergely, J.-L., Kolodziejczyk, N., Reverdin, G., Reul, N., & Tarasenko, A. (2020b). SMOS ARCTIC SSS L3 maps produced by CATDS CEC LOCEAN. *SEANOE*. https://doi.org/10.17882/71909

Tang, W., Yueh, S., Fore, A., Hayashi, A., & Steele, M. (2021). An empirical algorithm for mitigating the Sea Ice Effect in SMAP radiometer for sea surface salinity retrieval in the Arctic seas. *IEEE Journal of Selected Topics in Applied Earth Observations and Remote Sensing*, *14*, 1–11997. https://doi.org/10.1109/JSTARS.2021.3127470

Tang, W., Yueh, S., Yang, D., Fore, A., Hayashi, A., Lee, T., et al. (2018). The potential and challenges of using soil moisture active passive (SMAP) sea surface salinity to monitor Arctic Ocean freshwater changes. *Remote Sensing*, *10*(6), 869. https://doi.org/10.3390/rs10060869

Tarasenko, A., Supply, A., Kusse-Tiuz, N., Ivanov, V., Makhotin, M., Tournadre, J., et al. (2021). Properties of surface water masses in the Laptev and the East Siberian seas in summer 2018 from in situ and satellite data. *Ocean Science*, *221–247*(1), 221–247. https://doi.org/10.5194/os-17-221-2021

Timmermans, M.-L., Proshutinsky, A., Golubeva, E., Jackson, J. M., Krishfield, R., McCall, M., et al. (2014). Mechanisms of Pacific summer water variability in the Arctic's central Canada basin. *Journal of Geophysical Research: Oceans*, *119*(11), 7523–7548. https://doi.org/10.1002/2014JC010273

Vazquez-Cuervo, J., Gentemann, C., Tang, W., Carroll, D., Zhang, H., Menemenlis, D., et al. (2021). Using saildrones to validate Arctic sea-surface salinity from the SMAP satellite and from ocean models. *Remote Sensing*, *13*(5), 831. https://doi.org/10.3390/rs13050831

Vinogradova, N., Lee, T., Boutin, J., Drushka, K., Fournier, S., Sabia, R., et al. (2019). Satellite salinity observing system: Recent discoveries and the way forward. *Frontiers in Marine Science*, *6*, 243. https://doi.org/10.3389/fmars.2019.00243

Woodgate, R., & Peralta-Ferriz, C. (2021). Warming and freshening of the Pacific inflow to the Arctic from 1990–2019 implying dramatic shoaling in Pacific winter water ventilation of the Arctic water column. *Geophysical Research Letters*, *48*(9), e2021GL092528. https://doi.org/10.1029/2021GL092528